

Quantitative lock-in thermography imaging of thermal-wave spatial profiles and thermophysical property measurements in solids with inner corner geometries using thermal-wave field theory

Cite as: J. Appl. Phys. **124**, 205106 (2018); <https://doi.org/10.1063/1.5055705>

Submitted: 10 September 2018 . Accepted: 30 October 2018 . Published Online: 28 November 2018

Mingfeng Wang,  Andreas Mandelis, Alexander Melnikov, and Chinhua Wang



View Online



Export Citation



CrossMark

ARTICLES YOU MAY BE INTERESTED IN

[Perspective: Principles and specifications of photothermal imaging methodologies and their applications to non-invasive biomedical and non-destructive materials imaging](#)

Journal of Applied Physics **124**, 160903 (2018); <https://doi.org/10.1063/1.5044748>

[Bayesian calibration of strength parameters using hydrocode simulations of symmetric impact shock experiments of Al-5083](#)

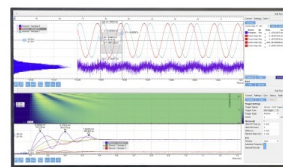
Journal of Applied Physics **124**, 205105 (2018); <https://doi.org/10.1063/1.5051442>

[Nano-scale wave dispersion beyond the First Brillouin Zone simulated with inertia gradient continua](#)

Journal of Applied Physics **124**, 205107 (2018); <https://doi.org/10.1063/1.5045838>

Challenge us.

What are your needs for periodic signal detection?



Zurich
Instruments



Quantitative lock-in thermography imaging of thermal-wave spatial profiles and thermophysical property measurements in solids with inner corner geometries using thermal-wave field theory

Mingfeng Wang,^{1,2,3} Andreas Mandelis,³ Alexander Melnikov,³ and Chinhua Wang^{1,2,a)}

¹*School of Optoelectronic Science and Engineering and Collaborative Innovation Center of Suzhou Nano Science and Technology, Soochow University, Suzhou 215006, China*

²*Key Lab of Advanced Optical Manufacturing Technologies of Jiangsu Province & Key Lab of Modern Optical Technologies of Education Ministry of China, Soochow University, Suzhou 215006, China*

³*Center for Advanced Diffusion-Wave and Photoacoustic Technologies (CADIPT), Department of Mechanical and Industrial Engineering, University of Toronto, Toronto, Ontario M5S 3G8, Canada*

(Received 10 September 2018; accepted 30 October 2018; published online 28 November 2018)

In this study, we established a theoretical photothermal model and its experimental validation for an infinitely long solid with an inner corner of arbitrary opening angle, with the solid being irradiated photothermally by a modulated laser beam of arbitrary spatial intensity distribution directed to the corner. The thermal-wave field distribution on the flat surfaces of the solid centered at the corner was obtained using the Green function method. Experimental results based on quantitative thermographic imaging were obtained and used to validate the theoretical model in which thermal diffusivity of an inner cornered stainless steel was measured. The thermal-wave theory based lock-in thermography imaging technique provides a quantitative tool for thermal property measurement and/or non-destructive evaluation of non-flat structures. It also generates valuable physical insights into the spatial distribution of the thermal-wave field in the neighborhood of geometric discontinuities such as inner corners in solids. *Published by AIP Publishing.* <https://doi.org/10.1063/1.5055705>

I. INTRODUCTION

Photothermal radiometry (PTR) has been a powerful tool for the thermophysical characterization and non-destructive evaluation (NDE) of broad classes of materials due to its noninvasive and highly sensitive nature. PTR was introduced by Nordal and Kanstad^{1,2} who derived analytical expressions for the PTR response signal and studied the physics and limitations of the PTR technique stemming from Planck's radiation law. Optimal measurement conditions have been discussed and experiments were carried out on various types of solid materials and devices such as solar cells, living plants, and hot objects using PTR.^{3–6} Photothermal imaging has proven to be well suited for many applications, with early PTR imaging⁷ accomplished through point-by-point scanning of the relative position of the illumination source (typically a laser) and a stationary or moving sample. However, the amount of time required for scanning large structures may be prohibitively long for practical applications, especially those aiming at imaging deep subsurface regions. In the 1990s, Busse *et al.* introduced lock-in thermography (LIT), an infrared camera based phase sensitive thermal wave imaging technique which greatly improves the image contrast, signal-to-noise ratio, and sample characterization speed.^{8,9}

Furthermore, due to the complex geometries of practical samples, thermal-wave field descriptions required for PTR

and LIT signal interpretation and sample parameter measurements are difficult to derive, thereby limiting detection to planar objects and restricting the extent of PTR and LIT technology applications. For example, thermal contact resistance measurements at a smooth polymer film and at a polished metal substrate interface were investigated early on using pulsed PTR.¹⁰ Lan *et al.*^{11,12} derived the surface thermal-wave field of a solid with linearly variable thermal conductivity as a function of depth and used their theory with experimental frequency-domain PTR data from conventional industrial hardened metallic and ceramic samples to reconstruct the depth profiles of the thermophysical properties of those samples. All the foregoing applications were based on planar one-dimensional models. With the recent growth in PTR and LIT applications for imaging characterization of materials, the demand for theoretical analysis of non-planar geometry measurements for thermophysical property extractions has also been growing. Wang *et al.*^{13–17} introduced analytical thermal-wave field representations of cylindrical and spherical geometries based on Green function formalisms¹⁸ and then used this method to study the PTR responses of surface-irradiated cylindrical and spherical solids. Salazar and Celorrio¹⁹ and Madariaga and Salazar²⁰ performed similar studies on multilayered cylindrical and spherical solids using the thermal quadrupole method. In comparison, the Green function method appears to be able to address the practical problem of inhomogeneous optical beam power profiles in a simpler and more straightforward manner. Using the Green function method, a solid-wedge sample was also characterized with frequency scanned PTR at a selected

^{a)}Author to whom correspondence should be addressed: chinhua.wang@suda.edu.cn

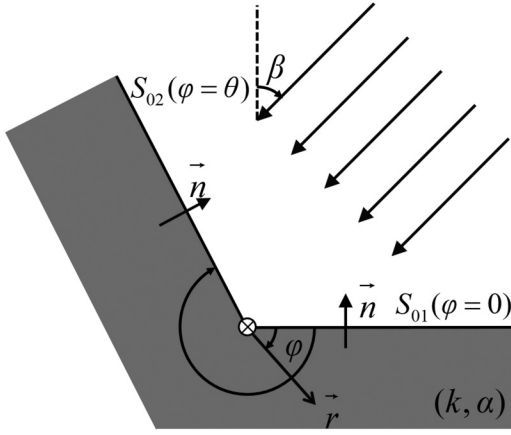


FIG. 1. Geometry and coordinates of a laser-beam-irradiated solid with an arbitrary inner opening angle.

single coordinate location.²¹ Yet, quantitative LIT imaging of non-planar geometries to-date is still rare. Therefore, in this work, we report a theoretical and experimental LIT imaging investigation of an angled corner structure with an arbitrary opening angle irradiated with an experimentally realistic nearly collimated, yet mildly divergent, laser beam. The theory is based on the Green function method.¹⁸

II. THERMAL-WAVE FIELD THEORY OF A SOLID CORNER

The geometry and cylindrical coordinates of a solid with an interior corner structure at the intersection of two open flat surfaces forming an arbitrary angle θ are shown in Fig. 1. In this geometry, the solid region of interest (ROI) spans angle θ and the opening corner spans angle $2\pi - \theta$. The thermal-wave field of the infinitely long cylindrical solid with an inner corner and infinite radius r , subject to inhomogeneous boundary conditions can be derived by means of the Green function method. The reflectivities of the two walls are R_1 and R_2 . The excitation light beam is directed to the inner surface of the solid at an arbitrary angle, β .

The harmonic thermal-wave equation for the material under investigation can be written as

$$\nabla^2 T(\vec{r}, \omega) - \sigma^2(\omega) \cdot T(\vec{r}, \omega) = -\frac{1}{k} Q(\vec{r}, \omega), \quad (1)$$

where $\sigma(\omega) = (i\omega/\alpha)^{1/2}$ is the complex thermal wavenumber, α (m^2/s) and k ($\text{W}/\text{m K}$) are, respectively, the thermal diffusivity and thermal conductivity of the material, ω is the angular modulation frequency of the laser beam, and $Q(\vec{r}, \omega)$ is the volume harmonic thermal-wave source at coordinates $\vec{r} = (r, \varphi)$ in the material. Based on the Green function method, the general solution for Eq. (1) can be expressed as¹⁸

$$\begin{aligned} T(\vec{r}, \omega) = & \frac{\alpha}{k} \iiint Q(\vec{r}_0, \omega) \cdot G(\vec{r} \rightarrow \vec{r}_0, \omega) \cdot dV_0 \\ & + \alpha \oint_{S_0} \left[G(\vec{r}|\vec{r}_0^s, \omega) \cdot \vec{\nabla}_0 T(\vec{r}_0^s, \omega) \right. \\ & \left. - T(\vec{r}_0^s, \omega) \cdot \vec{\nabla}_0 G(\vec{r}|\vec{r}_0^s, \omega) \right] \cdot d\vec{S}_0, \quad (2) \end{aligned}$$

where S_0 is the surface surrounding the domain volume V_0 that includes the harmonic source $Q(\vec{r}_0, \omega)$; \vec{r}_0^s is the source coordinate point on the surface S_0 . $d\vec{S}_0$ indicates an infinitesimal area vector along the outward normal to the boundary surface S_0 : $d\vec{S}_0 = \vec{n} dS_0$, with \vec{n} being the outward unit vector, as shown in Fig. 1. $G(\vec{r}|\vec{r}_0, \omega)$ is the thermal-wave Green function with units of (s/m^3). The general case, Eq. (2), can be simplified depending on specific material properties and boundary conditions imposed on the solid. For solids with high optical absorption coefficients, such as metals, the volume source can be neglected: $Q(\vec{r}_0, \omega) \equiv 0$. This is the case in this analysis where we will focus on metallic (opaque) solids which are purely surface absorbers. Moreover, considering that surface illumination by a laser beam leads to optical-to-thermal energy conversion essentially entirely on the surface and that the thermal coupling coefficient between a metallic solid and the surrounding gas (air) is in the order of 10^{-3} ,²² the adiabatic second-kind (Neumann) boundary condition at the external surface can be applied to a high degree of accuracy. The homogeneous boundary conditions for the appropriate Green function and the associated inhomogeneous conditions of the TW field function can be written, respectively, as

$$k\vec{n} \cdot \nabla G(\vec{r}|\vec{r}_0, \omega)|_{\varphi_0=\varphi_{01}, \varphi_{02}} = 0, \quad (3)$$

$$\begin{aligned} k\vec{n} \cdot \nabla T(\vec{r}|\vec{r}_0, \omega)|_{\varphi_0=\varphi_{01}, \varphi_{02}} \\ = (1 - R|_{R=R_1, R_2}) F_0(\vec{r}|\vec{r}_0, \omega)|_{\varphi_0=\varphi_{01}, \varphi_{02}}, \quad (4) \end{aligned}$$

where F_0 is the photothermal heat flux (W m^{-2}) imposed on the surface, and $\varphi_{01} = 0$, $\varphi_{02} = \theta$. Therefore, in the absence of volume thermal-wave sources in the solid structure of Fig. 1, and with the homogeneous boundary conditions for the Green function shown in Eq. (3), the general thermal-wave field represented by Eq. (2) for the axially infinitely long cylinder reduces to

$$\begin{aligned} T(\vec{r}, \omega) = \alpha \left[\oint_{S_{01}} F_1(\vec{r}_0, \omega) \cdot G(\vec{r}|\vec{r}_0, \omega) \cdot d\vec{S}_{01} \right. \\ \left. + \oint_{S_{02}} F_2(\vec{r}_0, \omega) \cdot G(\vec{r}|\vec{r}_0, \omega) \cdot d\vec{S}_{02} \right], \quad (5a) \end{aligned}$$

where

$$\begin{aligned} F_1 = F_0(1 - R_1) \cos(\beta) \text{ and } F_2 \\ = F_0(1 - R_2) \cos(\theta - \beta) \quad (5b) \end{aligned}$$

are the photothermal fluxes incident on the two angled surfaces and are generally presumed to be different. $G(\vec{r}|\vec{r}_0, \omega)$ must be derived so as to satisfy the appropriate homogeneous boundary conditions on all surfaces enclosing the volume V_0 .¹⁸

Details of the derivation of the Green function for the specified geometry are given in Appendix A. In summary, the appropriate Green function to be used in Eq. (5) was derived and can be written in terms of the observation coordinate, r , in the form

$$G(\vec{r}|\vec{r}_0, \omega) = \frac{1}{\alpha\theta} \times \begin{cases} I_0(\sigma r)K_0(\sigma r_0) + 2 \sum_{n=1}^{\infty} I_{\mu_n}(\sigma r)K_{\mu_n}(\sigma r_0) \cos(\mu_n \phi) \cos(\mu_n \phi_0), & 0 \leq r \leq r_0 \\ I_0(\sigma r_0)K_0(\sigma r) + 2 \sum_{n=1}^{\infty} I_{\mu_n}(\sigma r_0)K_{\mu_n}(\sigma r) \cos(\mu_n \phi) \cos(\mu_n \phi_0), & r_0 \leq r \leq \infty \end{cases}, \quad (6)$$

where $\mu_n = n\pi/\theta$ and r_0 is the source variable to be integrated over the surfaces of the solid on which the laser beam impinges.

Due to the assumed uniform illumination over the entire inner surface (wall and flat bottom), the geometry can be simplified to that of a random cross section of the solid as follows: the photothermal source is a heated strip on the surface $\varphi_{01} = 0$ and another strip on the surface $\varphi_{02} = \theta$; in both cases, the 2D source consists of two lines, on both sides along $0 \leq r < \infty$ so that the surface integral degenerates to a line integral. In other words, the outer edges of the angled solid surfaces are too far away from the illuminated region and are therefore ignored.

If a uniform exciting laser beam generates thermal-wave flux F_0 at an incident angle β , and the Green function [Eq. (6)] which is obtained according to the corresponding boundary conditions is substituted into Eq. (5), the thermal-wave field anywhere on the inner surface and inside the solid as a function of arbitrary thermal-wave fluxes F_1 and F_2 is given as

$$T(r, \varphi; \omega) = \frac{1}{\theta} [T_0(r, \varphi; \omega) + T_\theta(r, \varphi; \omega)], \quad (7)$$

with the definitions

$$T_0(r, \varphi; \omega) \equiv K_0(\sigma r) \int_0^r I_0(\sigma r_0) F_1(\vec{r}_0, \omega) dr_0 + I_0(\sigma r) \int_r^\infty K_0(\sigma r_0) F_1(\vec{r}_0, \omega) dr_0 \\ + 2 \sum_{n=1}^{\infty} I_{\mu_n}(\sigma r) \cos(\mu_n \phi) \int_r^\infty K_{\mu_n}(\sigma r_0) F_1(\vec{r}_0, \omega) dr_0 + 2 \sum_{n=1}^{\infty} K_{\mu_n}(\sigma r) \cos(\mu_n \phi) \int_0^r I_{\mu_n}(\sigma r_0) F_1(\vec{r}_0, \omega) dr_0 \quad (8a)$$

and

$$T_\theta(r, \varphi; \omega) \equiv K_0(\sigma r) \int_0^r I_0(\sigma r_0) F_2(\vec{r}_0, \omega) dr_0 + I_0(\sigma r) \int_r^\infty K_0(\sigma r_0) F_2(\vec{r}_0, \omega) dr_0 \\ + 2 \sum_{n=1}^{\infty} I_{\mu_n}(\sigma r) \cos(\mu_n \phi) \cos(n\pi) \int_r^\infty K_{\mu_n}(\sigma r_0) F_2(\vec{r}_0, \omega) dr_0 + 2 \sum_{n=1}^{\infty} K_{\mu_n}(\sigma r) \cos(\mu_n \phi) \cos(n\pi) \int_0^r I_{\mu_n}(\sigma r_0) F_2(\vec{r}_0, \omega) dr_0. \quad (8b)$$

Inserting Eqs. (8a) and (8b) back into Eq. (7) yields the following expression for the thermal-wave field generated by the specific thermal-wave fluxes of Eq. (5b) at any point in the material:

$$T(r, \varphi; \omega) \equiv \frac{1}{\theta} [K_0(\sigma r) \int_0^r I_0(\sigma r_0) [F_1(\vec{r}_0, \omega) + F_2(\vec{r}_0, \omega)] dr_0 \\ + 2 \sum_{n=1}^{\infty} I_{\mu_n}(\sigma r) \cos(\mu_n \phi) \int_r^\infty K_{\mu_n}(\sigma r_0) [F_1(\vec{r}_0, \omega) + \cos(n\pi) F_2(\vec{r}_0, \omega)] dr_0 + I_0(\sigma r) \int_r^\infty K_0(\sigma r_0) [F_1(\vec{r}_0, \omega) \\ + F_2(\vec{r}_0, \omega)] dr_0 + 2 \sum_{n=1}^{\infty} K_{\mu_n}(\sigma r) \cos(\mu_n \phi) \int_0^r I_{\mu_n}(\sigma r_0) [F_1(\vec{r}_0, \omega) + \cos(n\pi) F_2(\vec{r}_0, \omega)] dr_0, \quad (9)$$

where the various symbols have been defined previously. In the case of vertical walls and an opening angle for 90° , $S_0 = S_{01}(\varphi_{01} = 0) + S_{02}(\varphi_{02} = \theta = 3\pi/2)$, so that $\mu_n = 2n/3$.

The following expressions can now be derived for the thermal-wave field along the directions of the two vertical corner walls:

(a) Along the horizontal plane S_{01} , $r = r_1$, $\varphi = 0$

$$\begin{aligned}
 T(r_1, 0; \omega) \equiv & \frac{2}{3\pi} [K_0(\sigma r_1) \int_0^{r_1} I_0(\sigma r_0) [F_1(\vec{r}_0, \omega) + F_2(\vec{r}_0, \omega)] dr_0 + 2 \sum_{n=1}^{\infty} I_{2n/3}(\sigma r_1) \int_{r_1}^{\infty} K_{2n/3}(\sigma r_0) [F_1(\vec{r}_0, \omega) \\
 & + (-1)^n F_2(\vec{r}_0, \omega)] dr_0 + I_0(\sigma r_1) \int_{r_1}^{\infty} K_0(\sigma r_0) [F_1(\vec{r}_0, \omega) + F_2(\vec{r}_0, \omega)] dr_0 + 2 \sum_{n=1}^{\infty} K_{2n/3}(\sigma r_1) \int_0^{r_1} I_{2n/3}(\sigma r_0) [F_1(\vec{r}_0, \omega) \\
 & + (-1)^n F_2(\vec{r}_0, \omega)] dr_0.
 \end{aligned} \tag{10a}$$

(b) Along the vertical plane S_{02} , $r = r_2$, $\varphi = 3\pi/2$

$$\begin{aligned}
 T(r_2, 3\pi/2; \omega) \equiv & \frac{2}{3\pi} [K_0(\sigma r_2) \int_0^{r_2} I_0(\sigma r_0) [F_1(\vec{r}_0, \omega) + F_2(\vec{r}_0, \omega)] dr_0 + 2 \sum_{n=1}^{\infty} I_{2n/3}(\sigma r_2) \int_{r_2}^{\infty} K_{2n/3}(\sigma r_0) [(-1)^n F_1(\vec{r}_0, \omega) \\
 & + F_2(\vec{r}_0, \omega)] dr_0 + I_0(\sigma r_2) \int_{r_2}^{\infty} K_0(\sigma r_0) [F_1(\vec{r}_0, \omega) \\
 & + F_2(\vec{r}_0, \omega)] dr_0 + 2 \sum_{n=1}^{\infty} K_{2n/3}(\sigma r_2) \int_0^{r_2} I_{2n/3}(\sigma r_0) [(-1)^n F_1(\vec{r}_0, \omega) + F_2(\vec{r}_0, \omega)] dr_0.
 \end{aligned} \tag{10b}$$

It should be noted that for equidistant radial locations from the corner, $r_1 = r_2 = r$, and in the special case where $F_1 = F_2$, the equality $T(r, 0; \omega) = T(r, 3\pi/2; \omega)$ can be proven, as expected physically from the symmetric illumination of both perpendicular plane surfaces.

III. NUMERICAL SIMULATIONS

Although Eqs. (10a) and (10b) explicitly demonstrate the relationship between the thermal-wave field and the material thermal diffusivity and conductivity, and several geometric and measurement configuration factors for a right-angled corner structure sample (i.e., $\theta = 3\pi/2$), the complicated functional dependence of the photothermal signal on the various system parameters makes any attempt for further understanding of the system behavior under a photothermal probe difficult. To gain more physical insights into the characteristics of the thermal-wave field, it is instructive to study its dependence on each individual parameter involved in Eqs. (10a) and (10b). Considering the nature of LIT as an imaging technique of surface thermal-wave distributions, only the field on the sample surface was evaluated. The back-propagation/diffusion (reflection) experimental configuration was used in this work. In the following simulation, modulated laser illumination was directed to the inner corner at 45° (i.e., $\beta = 45^\circ$) and the mid-infrared camera was assumed tilted also at 45° , so both surfaces of the right-angle corner were illuminated uniformly.

Figures 2(a) and 2(b) show the theoretical LIT signal behavior of a corner structure in a solid sample at several modulation frequencies measured on the surface ($\varphi = 0$). Figures 2(c) and 2(d) show the effect of material thermal diffusivity variation on the thermal-wave field measured on the

surface ($\varphi = 0$) at 1.2 Hz. The material parameters of the corner structure (stainless steel AISI304 is assumed) used in the simulation were as follows: $\alpha = 4.05 \times 10^{-6} \text{ m}^2/\text{s}$,²² $F_0 = 1 \text{ W/cm}^2$ (absolute value of F_0 has no effect on the thermal-wave distribution). The amplitude and phase were self-normalized in that amplitude was divided by the first point, i.e., the amplitude at $r = 0$, and the phase was subtracted from the phase at $r = 0$. It is seen that both amplitudes and phases are sensitive to the value of the modulation frequency and thermal diffusivity: As frequency increases or diffusivity decreases, the peak/valley positions of the amplitude and phase distributions shift toward shorter radial locations away from the corner. This correspondence between frequency and diffusivity is expected from the structure of the thermal wavenumber, the main parameter controlling the behavior of the thermal-wave field. These maxima are the result of self-interference between the two branches of coherent thermal-waves photothermally launched on both sides of the corner wall. As the thermal wavenumber increases, this effect becomes confined closer to the origin at $r = 0$, an effect that amounts to higher spatial resolution of the LIT image. Amplitude and phase also change dramatically with the opening angle. Figures 3(a) and 3(b) show the effect of opening angle θ [using Eq. (9)] on the thermal-wave field measured on the sample surface ($\varphi = 0$) at 1.2 Hz. The material parameters used in the simulation and the normalization process of amplitude and phase are the same as those in Fig. 2. It is observed that the curvatures of the radial distributions change sign on either side of the case $\theta = \pi$ (a uniformly illuminated continuous plane surface). The simulations of Figs. 2 and 3 yield valuable physical insights into the behavior and spatial distribution of thermal waves in solids with sharp inner boundaries and material discontinuities like

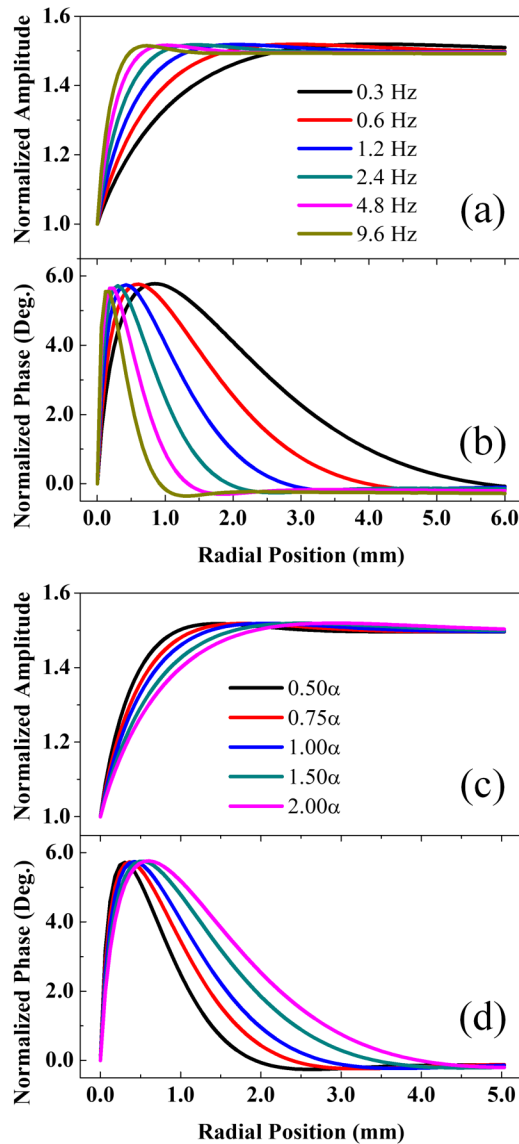


FIG. 2. Theoretical amplitude and phase curves for various frequencies and thermal diffusivities as functions of radial coordinate. Amplitudes and phases are normalized to their values (self-normalized) at the origin $r = 0$.

corners. The presence of the vertical corner ($\theta = 270^\circ$) walls at the origin, when compared to plane surfaces, represents a sudden increase in the extent of the solid medium beyond the confines of each wall which maintains the thermal-wave amplitude high. It is interesting to observe the thermal-wave interference patterns (weak amplitude maxima) in Fig. 2 near the wall within distances comparable to the thermal diffusion length. They are the result of coherent superposition of accumulating thermal waves against the wall surface and the forward diffusing thermal waves toward that direction. However, at distances shorter than the interference maximum locations, additional diffusion/propagation degrees of freedom (DOFs) beyond the vertical wall and into the other side of the corner emerge and dominate the wall-originated confinement. As a result, the thermal-wave amplitude plunges in the neighborhood of the origin while the phase lag sharply increases as the thermal wave spreads into the other side away from the origin. Figure 3

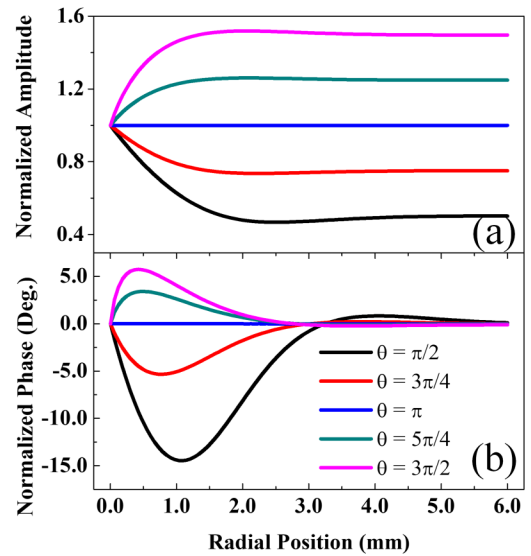


FIG. 3. Theoretical amplitude and phase curves for various opening angles as functions of radial coordinate. Amplitudes and phases are normalized to their values (self-normalized) at the origin $r = 0$.

clearly shows the effects of asymmetry of the thermal-wave distributions with the same optical source incidence at several opening angles: The thermal-wave field at an inner right corner ($\theta = 270^\circ$) is *not* the symmetric counterpart of the field generated inside a $\theta = 90^\circ$ right edge. In the former case, the two vertical walls of the right-angle corner produce the aforementioned thermal-wave patterns with the amplitude decrease near the origin. In the latter case, the solid right edge represents a double confinement region of thermal waves generated on both side walls and the superposition amplitude increases with decreasing distance from the origin. Besides their intrinsic theoretical and physical interest, these radial distributions can be used to evaluate the effective photothermal behavior of inner corner structures under optical irradiation for practical applications of the non-destructive LIT technique.

IV. EXPERIMENTAL RESULTS AND DISCUSSION

To verify the foregoing theoretical model, LIT imaging experiments were performed using a corner structure sample (made of stainless steel AISI304) with fixed $\theta = 3\pi/2$ (a 90° corner when viewed from the outside). Figures 4(a) and 4(b) show the schematic diagram of the LIT imaging setup and configuration. A semiconductor laser (~ 40 W, 808 nm) was used as the (photo)thermal-wave source. The output of the laser was modulated by a periodic voltage, the modulation frequency of which was controlled by a computer which also served as the lock-in reference. The laser beam was expanded and collimated onto the surface of the sample with a spot size of ~ 40 mm. The harmonically modulated infrared radiation emitted from the sample surface was detected by a mid-infrared camera (Cedip Titanium model 520M). All measurements were carried out at room temperature (300 K). Modulated laser illumination was directed to the inner corner at $\beta = 45^\circ$ and the mid-infrared camera was also tilted at $\beta = 45^\circ$, so both surfaces of the right-angle corner were

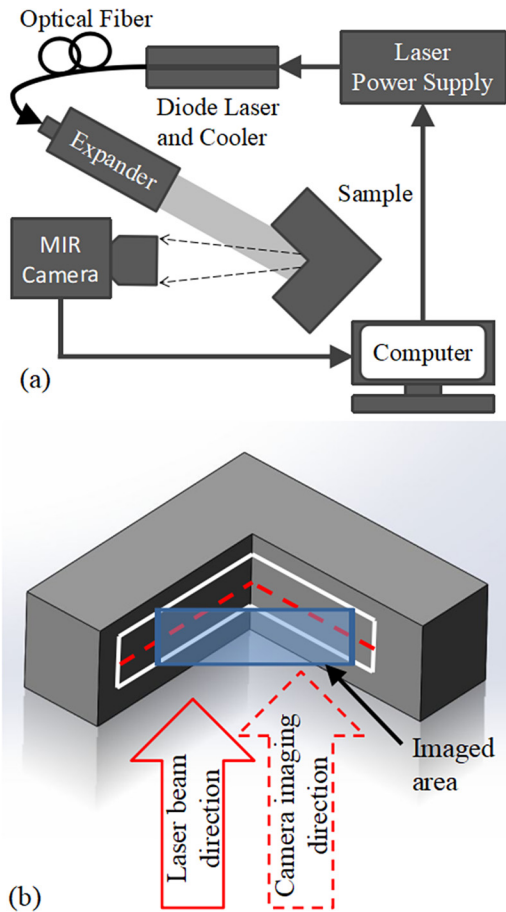


FIG. 4. (a) Schematic diagram of the LIT imaging experimental setup; (b) schematic diagram of the imaging configuration.

illuminated symmetrically. The computer received the camera signals, the latter being connected to it through a data acquisition interface (National Instruments, NI USB 6229). Then a LABVIEW digital lock-in algorithm was used to process data and demodulate pixel signals in the form of amplitude and phase images. The blue box in Fig. 4(b) delineates the area the camera could detect and the red dashed line represents the pixel row of data used for fitting the theory to the data.

Figure 5 shows the demodulated amplitude and phase images obtained from the steel sample in a quantitative manner. From Figs. 5(a) to 5(f), the horizontal and vertical axes are the pixels of the camera, with color coding of the amplitude and phase values. To compare with the theory, pixel row data were selected along the horizontal red line in Fig. 4(b) and were self-normalized as defined below. Taking into account the symmetry of both sides, only data of the 80th row of a total of 160 rows on one side of the corner were considered. Figures 5(g) and 5(h) show linescans of the amplitude and phase of the 80th row in the image. The amplitude and phase are self-normalized, i.e., the group of pixel-row signal amplitudes was divided by the maximum amplitude, and from the group of phases, the minimum phase was subtracted. The self-normalized method was found to be useful for minimizing noise and eliminating the background of the experimental results. It should be noted that

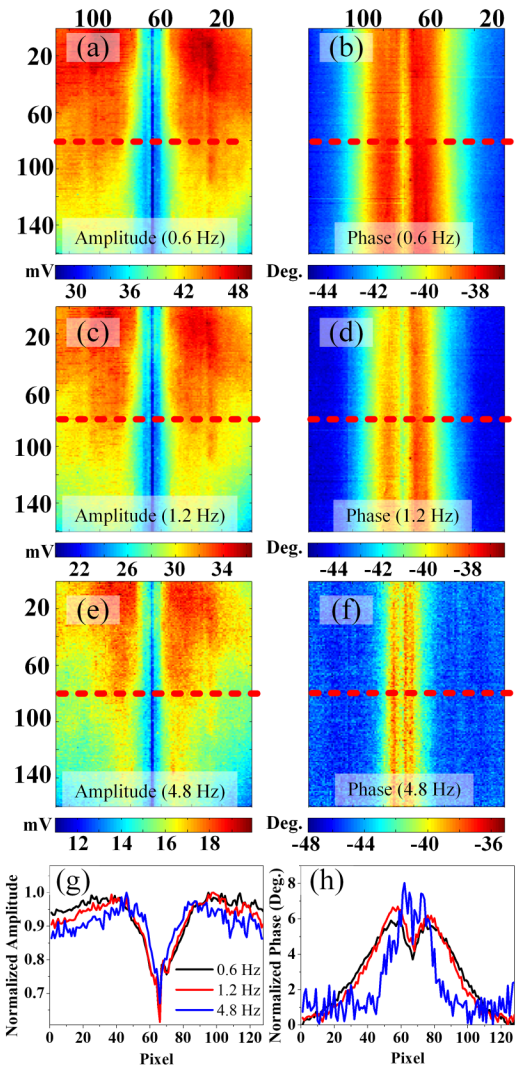


FIG. 5. LIT amplitude [(a), (c), and (e)] and phase [(b), (d), and (f)] images of the inner corner at 0.6 Hz, 1.2 Hz, and 4.8 Hz. Line scans of amplitude (g) and phase (h) at the pixel row # 80.

the number of pixels in Fig. 5 must be calibrated into the absolute length or coordinate (i.e., r in the theory) in order to quantitatively fit the experimental data to theory. The calibration of the camera pixel array to the absolute coordinates on the sample surface was easily performed by placing a Vernier caliper in front of the camera at the same position as the sample. In this manner, the length on the caliper corresponding to the number of pixels could be precisely obtained, and subsequently the length corresponding to each pixel (i.e., calibration constant a , in units of m/pixel) could be calculated. Furthermore, considering the fact that the surface of the sample was at an angle of 45° with respect to the axis of the camera lens, the absolute coordinate on the slanted surface must be calculated considering the effect of projection from the camera pixels to the coordinate length on the surface. The relationship among the length (coordinate) on the surface (r), calibration constant (a), slant angle of the surface ($\pi - \theta/2$), and the number of pixels (P) are $r = Pa / \cos(\pi - \theta/2)$. The calculated r was used in the fitting process as shown in Eqs. (10a) or (10b). It should be emphasized that the accuracy of the conversion process from pixel

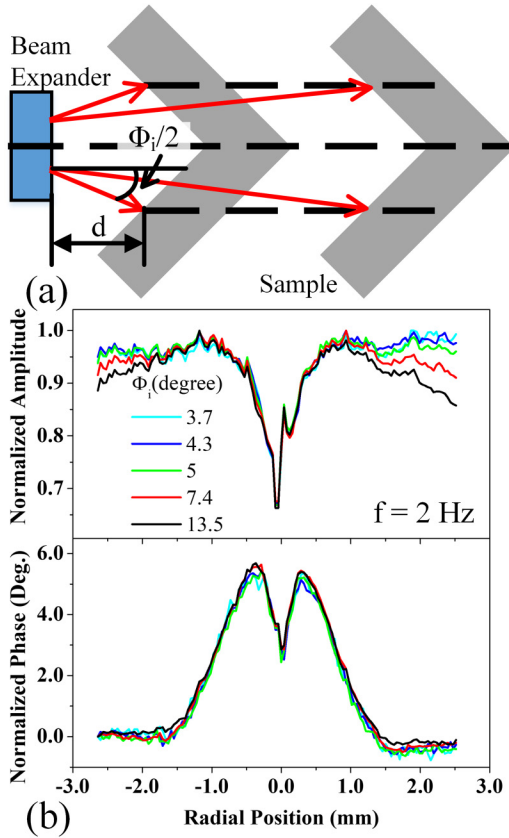


FIG. 6. (a) Schematic diagram of the experimental setup for exploring the effect of beam divergence angle on the LIT image. d : distance between expander and sample; Φ_i : divergence angle. (b) Experimental amplitude and phase at various divergence angles obtained at 2 Hz.

number (P) to the coordinate length (r) directly affects the best-fitted value of thermal diffusivity, which can also be seen from the structure of Eqs. (10a) and (10b) in that thermal diffusivity and coordinate length appear together as a product.

It was found that the experimental data showed an increasing divergence from the theory with increasing radial distance from the origin at $r=0$, as seen in Fig. 2 with a declining amplitude with increased r . To identify the source of this discrepancy, several groups of experiments were carried out. Among the various possibilities, the mild divergence of the laser beam past the expander, Fig. 4(a), was found to be the most likely source of the radial disagreement with the theory of Eqs. (8–10). It should be recalled that the thermal-wave theory that led to those equations assumed uniform surface irradiation.

To verify the effect of the divergence angle of the expanded laser beam on the amplitude and phase images, further experimental confirmation was sought. Figure 6(a) shows the schematic of the experimental measurement when a diverging laser beam is incorporated. Figure 6(b) shows the self-normalized amplitude and phase when the corner sample was placed at different distances from the beam expander. The divergence angle Φ_i of the excitation beam impinging on the interrogated surface is a function of the distance d between the sample and the beam expander: d can be varied and Φ_i calculated for each value of d . In our experiment, the

maximum Φ_i was around 20° . It is seen from Fig. 6(b) that when the divergence angle Φ_i increases, the amplitude decreases at large distances from the corner origin: the greater the value of Φ_i , the steeper the amplitude decline. However, the phase does not change significantly with Φ_i .

In what follows, the thermal-wave theory was generalized to include the effect of variable optical source intensity profiles. Essentially, the diverging angle geometry renders the incident optical flux F_0 a function of r , rather than a constant over r when the incident light is a collimated beam as assumed in the theoretical simulation of Fig. 2. Using

$$F = \frac{P}{S}, \quad (11)$$

where F is the laser intensity, P is the power, and S is the irradiated area, and introducing a geometric optics model of light ray propagation in a planar geometry, the expression of modified intensity can be shown to be

$$F(r) = I_0 \cos \frac{\pi}{4} \cdot [1 - C_1 \tan(C_2 r)]. \quad (12)$$

Here, $C_1 = (L_x/x)\cos(\pi/4)$, $C_2 = (1/L_j)\cos(\pi/4)$, and I_0 is the laser intensity without beam divergence (a constant); x is the half width of the non-diverged laser beam as it emerges from the expander; L_x is the distance between the expander and the outer edge of the divergent beam at the intersection with the solid wall; and L_j is the distance between the expander and the edge of the non-divergent (ideally collimated) beam at the intersection with the solid wall. The geometric schematic and details of the derivation of Eq. (12) are given in Appendix B.

Introducing Eq. (12) inside the radial integrals of Eq. (10) to replace the (previously assumed constant) fluxes F_1 and F_2 gives a generalized thermal-wave theory of the LIT imaging system under a diverging laser-beam illumination. Based on the generalized theory of Eqs. (10) and (12), best fits to the radial distribution of the camera LIT signals from the selected pixel row were conducted using either the amplitude or the phase data from the three frequencies shown in Fig. 5. Figure 7 shows that the generalized theoretical amplitude and phase curves fit the experimental data very well. In the fitting process, the thermal diffusivity and C_1 and C_2 were assumed to be best-fit parameters in the MATLAB program. The theoretical values were also self-normalized for consistency and comparison. It is noted that the origin of the coordinate system (i.e., zero point of the coordinate, r) must also be determined when the imaging data are used in the theoretical fitting. There is a difference (offset Δr) between the theoretical origin and the starting point in the imaging data. The offset of the origin Δr was determined as a fitting parameter. In the fitting process, three sets of experimental data at frequencies $f=0.6, 1.2,$ and 4.8 Hz shown in Fig. 5 were fitted to the theory as a whole using one set of fitting parameters ($\alpha, C_1, C_2, \Delta r$) considering the fact that all the data at different frequencies were taken from the same material. The best-fit results yielded $\alpha = 4.2 \times 10^{-6} \text{ m}^2/\text{s}$, $C_1 = 3.5$, $C_2 = 6$, and $\Delta r = 1 \times 10^{-5} \text{ m}$. According to published data,²² the thermal diffusivity of AISI304 steel is $3.95 \times 10^{-6} \text{ m}^2/\text{s}$ at 300 K and $4.08 \times 10^{-6} \text{ m}^2/\text{s}$ at 400 K. In the experiment, the

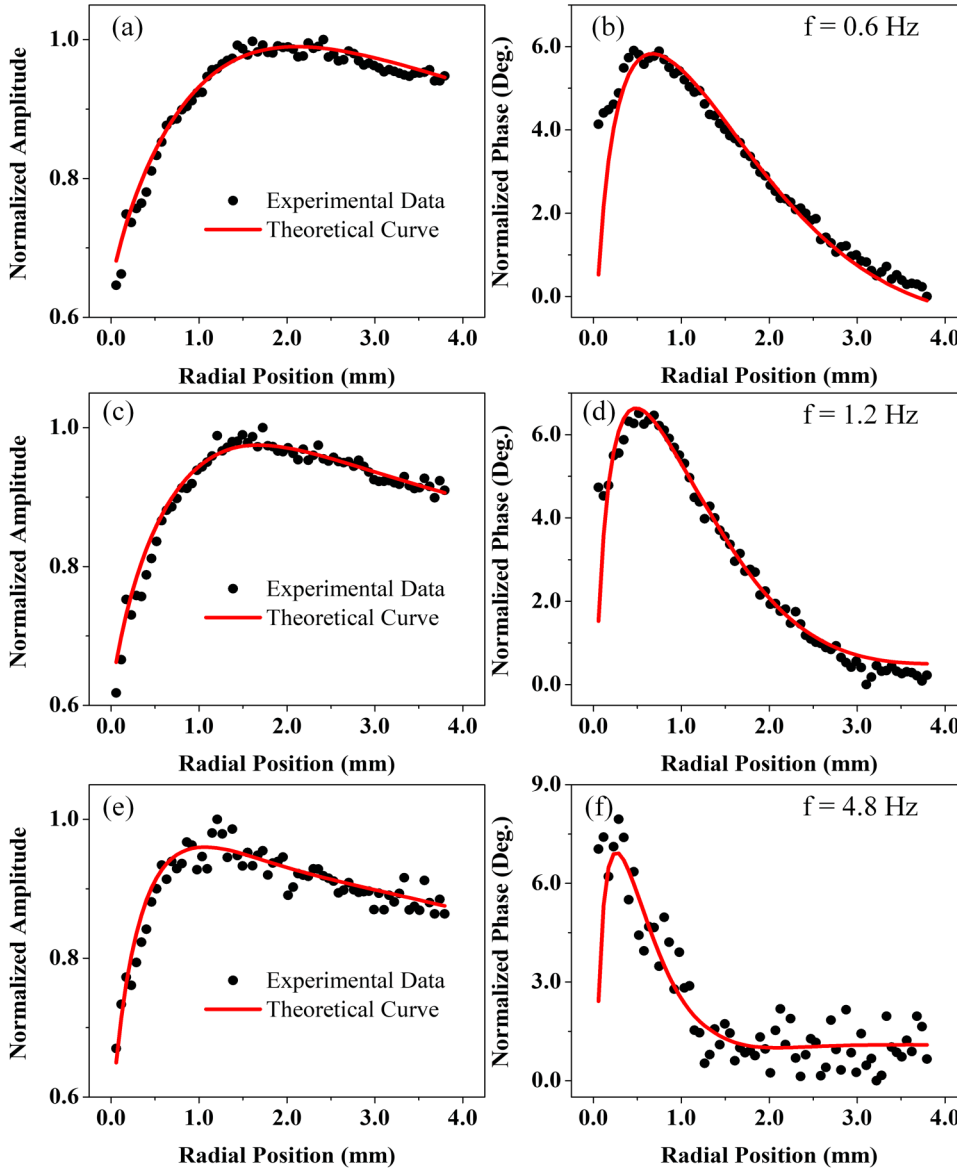


FIG. 7. Experimental results and the corresponding generalized theoretical model fits for the AISI 304 steel sample at 0.6 Hz, 1.2 Hz, and 4.8 Hz.

actual temperature of the sample after being irradiated by the laser was 330 K. The calculated thermal diffusivity at 330 K is $3.99 \times 10^{-6} \text{ m}^2/\text{s}$ if a linear relation is assumed, the error being 5% compared to the best-fitted value.

The fitting error at each frequency was estimated using the square root of the ratio of the average deviation between the experimental data and the theoretical fits to the normalized amplitude and phase, i.e.,

$$\text{error} = \sqrt{\frac{\sum_{i=1}^2 \sum_{j=1}^N [P_{i,fit}(f_j) - P_{i,e}(f_j)]^2}{\sum_{j=1}^N [P_{i,e}(f_j)]^2}}, \quad (13)$$

where $i=1$ and 2 represent the amplitude and the phase, respectively. N is the total number of data points. $P_{i,e}(f_j)$ denotes the experimental amplitude and phase, and $P_{i,fit}(f_j)$ denotes the amplitude and phase calculated with the theoretical model. The root-mean-square (rms) errors between the theoretical value (amplitude and phase) and the experimental

data were 0.026, 0.016, and 0.093 at 0.6 Hz, 1.2 Hz, and 4.8 Hz, respectively. The error at each frequency is very small and the experimental results fit the theoretical curve very well. This model can be widely used in the field of infrared nondestructive testing under experimentally realistic conditions.

V. CONCLUSIONS

In summary, we have formulated a new generalized thermal-wave model that is suitable for quantitative characterization of solids with arbitrary inner angle openings irradiated with diverging or otherwise inhomogeneous laser beams using lock-in thermography (LIT) imaging. Expressions for the thermal-wave field distribution on the surface of the solid were obtained using the thermal-wave Green function method. The influence of the excitation light beam divergence angle on the amplitude was found to be necessary to incorporate into the theory, and the generalized model was verified by best fitting the radial thermal-wave field away from the corner origin to the LIT data from the infrared

camera. The theoretical model yielded valuable physical insights into the behavior of thermal-wave fields in the neighborhood of, and across, abrupt material geometric discontinuities such as an inner corner. The thermal diffusivity of the solid was also extracted from the corner thermal-wave field measurements along single-line radial pixel profiles in the irradiated area. This method allows the reconstruction of thermophysical parameter images in non-planar solids.

ACKNOWLEDGMENTS

The National Natural Science Foundation of China (NNSFC) (No.61775154) and a project funded by the Priority Academic Program Development of Jiangsu Higher Education Institutions (PAPD) are acknowledged. A. Mandelis and A. Melnikov are grateful to the Natural Sciences and Engineering Research Council of Canada (NSERC) for a Discovery Grant and to the Canada Research Chairs program.

APPENDIX A: THERMAL-WAVE (TW) GREEN FUNCTION FOR AN ANGLED CORNER STRUCTURE

Here, we calculate the Green function for a cylindrical sector of infinite height, radius R , opening angle θ , and a cylindrical-strip thermal wave source located at $r=r_0$. Homogeneous Neumann conditions are prescribed at $r=R$ and $\varphi=0, \theta$.

A cross-sectional view of the infinite-height geometry is shown in Fig. 8. The TW Green function satisfies the equation

$$\frac{1}{r} \frac{\partial}{\partial r} \left[r \frac{\partial}{\partial r} G(\vec{r}|\vec{r}_0; \omega) \right] + \frac{1}{r^2} \frac{\partial^2}{\partial \varphi^2} G(\vec{r}|\vec{r}_0; \omega) - \sigma^2 G(\vec{r}|\vec{r}_0; \omega) = -\frac{\delta(r-r_0)\delta(\varphi-\varphi_0)}{\alpha r}. \quad (\text{A1})$$

This is a two-dimensional version of the more complete three-dimensional cylindrical coordinate equation. The homogeneity of the spatially impulsive source along the z axis renders the Green function independent of the coordinate z . Separation of variables $G(r, \varphi|r_0; \omega) = R(r)\Phi(\varphi)$ for all points $r \neq r_0$ leads to the ordinary differential equations

$$r \frac{d}{dr} \left[r \frac{dR(r)}{dr} \right] - (\sigma^2 r^2 + \lambda^2) R(r) = 0 \quad (\text{A2})$$

and

$$\frac{d^2 \Phi(\varphi)}{d\varphi^2} + \lambda^2 \Phi(\varphi) = 0. \quad (\text{A3})$$

The solution to the boundary-value problem consisting of Eq. (A3) plus homogeneous Neumann boundary conditions at $\varphi=0, \theta$ is the eigenfunction set

$$\Phi_n(\varphi) = A_n \cos(\lambda_n \varphi), \lambda_n = \frac{n\pi}{\theta}, n = 0, 1, 2, \dots \quad (\text{A4})$$

The solution to the radial equation can be written in

terms of two linearly independent function families

$$R_n(r) = B_n I_{\lambda_n}(\sigma r) + C_n K_{\lambda_n}(\sigma r), \quad (\text{A5})$$

where $I_{\lambda_n}(\sigma r)$ and $K_{\lambda_n}(\sigma r)$ are modified Bessel functions of the first and the second kind, respectively, of non-integer order λ_n and of complex argument. Representations and approximations of these functions are given in Abramowitz and Stegun.²³ Summing up over the complete eigenfunction set $\{\cos(\lambda_n \varphi)\}$, we may express the Green function as

$$G_{<}(r, \varphi|\vec{r}_0; \omega) = \sum_{n=0}^{\infty} a_n I_{\lambda_n}(\sigma r) \cos(\lambda_n \varphi), 0 \leq r \leq r_0, \quad (\text{A6a})$$

$$G_{>}(r, \varphi|\vec{r}_0; \omega) = \sum_{n=0}^{\infty} [b_n I_{\lambda_n}(\sigma r) + c_n K_{\lambda_n}(\sigma r)] \times \cos(\lambda_n \varphi), r_0 \leq r \leq R, \quad (\text{A6b})$$

where $G_{<}$ stands for the inner solution below the synco-pated tangential line and $G_{>}$ stands for the outer solution above the line in Fig. 8.

As usual, we require continuity of the Green function at $r=r_0$,

$$G_{<}(r, \varphi|\vec{r}_0; \omega) = G_{>}(r, \varphi|\vec{r}_0; \omega), \quad (\text{A7})$$

and discontinuity of its radial derivative

$$\frac{\partial}{\partial r} G_{>}(r, \varphi|\vec{r}_0; \omega)|_{r=r_0} - \frac{\partial}{\partial r} G_{<}(r, \varphi|\vec{r}_0; \omega)|_{r=r_0} = -\frac{\delta(\varphi-\varphi_0)}{\alpha r_0}. \quad (\text{A8})$$

The exterior homogeneous Neumann boundary condition $\partial G_{>}(r, \varphi|r_0; \omega)/\partial r|_{r=R} = 0$ can be used to determine each and every partial thermal-wave coefficient set (a_n, b_n, c_n) . This is done in a straightforward manner if Eqs. (A6a) and (A6b) are inserted in Eq. (A1), and the angular completeness relation,¹⁸

$$\delta(\varphi-\varphi_0) = \frac{1}{\theta} \left[1 + 2 \sum_{n=1}^{\infty} \cos\left(\frac{n\pi\varphi}{\theta}\right) \cos\left(\frac{n\pi\varphi_0}{\theta}\right) \right], \quad (\text{A9})$$

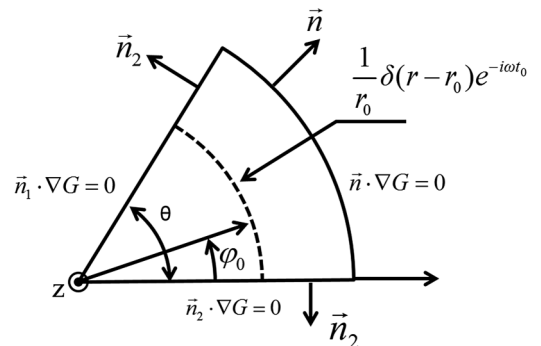


FIG. 8. Cross section of a corner structure for calculating the Green function.

is also used to expand the Dirac delta function $\delta(\varphi - \varphi_0)$. It is found that the term $n=0$ must be taken separately from the $n>0$ term due to the different relative weight of the $n=0$ versus $n>0$ terms in the $\delta(\varphi - \varphi_0)$ expansion above. In deriving the Green-function coefficients in (A6a) and (A6b), the following Wronskian identity is used:

$$W[K_\nu(z), I_\nu(z)] = K_\nu(z)I_{\nu+1}(z) + K_{\nu+1}(z)I_\nu(z) = \frac{1}{z}. \quad (\text{A10})$$

In addition, the general recurrence relations can be used to show that for any integer and non-integer ν ,

$$K'_\nu(\sigma r_0) = -\sigma K_{\nu+1}(\sigma r_0) + \frac{\nu}{r_0} K_\nu(\sigma r_0), \quad (\text{A11})$$

$$I'_\nu(\sigma r_0) = \sigma I_{\nu+1}(\sigma r_0) + \frac{\nu}{r_0} I_\nu(\sigma r_0), \quad (\text{A12})$$

where $I'_\nu(\sigma r_0) = dI_\nu(\sigma r_0)/dr|_{r=r_0}$. These relations can be used to prove the identity

$$I_{n\pi/\theta}(\sigma r_0)K'_{n\pi/\theta}(\sigma r_0) - K_{n\pi/\theta}(\sigma r_0)I'_{n\pi/\theta}(\sigma r_0) = -\frac{1}{r_0}. \quad (\text{A13})$$

Finally, the complete expression for the thermal-wave Green function in the domain of the cylindrical wedge of Fig. 8 is derived as follows:

$$G(\vec{r}|\vec{r}_0, \omega) = \frac{1}{\alpha\theta} \times \begin{cases} \frac{I_0(\sigma r)}{I'_0(\sigma R)} [I'_0(\sigma R)K_0(\sigma r_0) - K'_0(\sigma R)I_0(\sigma r_0)] \\ + 2 \sum_{n=1}^{\infty} \left\{ \frac{I_{n\pi/\theta}(\sigma r)}{I'_{n\pi/\theta}(\sigma R)} \times [I'_{n\pi/\theta}(\sigma R)K_{n\pi/\theta}(\sigma r_0) \right. \\ \left. - K'_{n\pi/\theta}(\sigma R)I_{n\pi/\theta}(\sigma r_0)] \times \cos\left(\frac{n\pi\varphi}{\theta}\right) \cos\left(\frac{n\pi\varphi_0}{\theta}\right) \right\}, 0 \leq r \leq r_0 \\ \frac{I_0(\sigma r_0)}{I'_0(\sigma R)} [I'_0(\sigma R)K_0(\sigma r) - K'_0(\sigma R)I_0(\sigma r)] \\ + 2 \sum_{n=1}^{\infty} \left\{ \frac{I_{n\pi/\theta}(\sigma r_0)}{I'_{n\pi/\theta}(\sigma R)} \times [I'_{n\pi/\theta}(\sigma R)K_{n\pi/\theta}(\sigma r) \right. \\ \left. - K'_{n\pi/\theta}(\sigma R)I_{n\pi/\theta}(\sigma r)] \times \cos\left(\frac{n\pi\varphi}{\theta}\right) \cos\left(\frac{n\pi\varphi_0}{\theta}\right) \right\}, r_0 \leq r \leq R \end{cases} \quad (\text{A14})$$

APPENDIX B: INTENSITY OF EXCITATION LASER SOURCE WITH BEAM DIVERGENCE

Figure 9 gives the geometry of a right-angled corner structure illuminated with a divergent laser beam incident at 45° with respect to both surfaces. When $r/L_j \ll 1$

$$\tan \theta = \frac{DE}{OE} = \frac{r \cos \frac{\pi}{4}}{L_j - r \cos \frac{\pi}{4}} \approx \frac{r}{L_j} \cos \frac{\pi}{4} / \left(1 - \frac{r}{L_j} \cos \frac{\pi}{4}\right) \approx \frac{r}{L_j} \cos \frac{\pi}{4}. \quad (\text{B1})$$

The coordinate y is perpendicular to the plane of the sheet

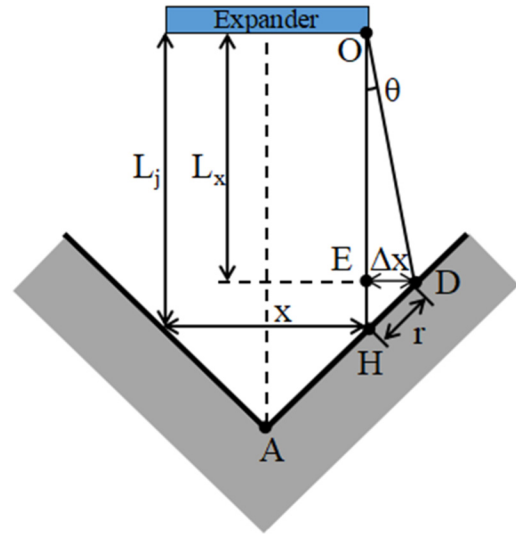


FIG. 9. Geometrical optics geometry of a right-angled corner structure illuminated with a divergent laser beam.

$$Intensity = F(AH + r) = \frac{P}{y(AH + r)} = \frac{P \cos \frac{\pi}{4}}{y(x + \Delta x)}. \quad (\text{B2})$$

Let

$$I_0 = \frac{P}{xy}, \quad (\text{B3})$$

where I_0 is a constant intensity corresponding to ideal fully collimated laser beam excitation. Inserting Eq. (B3) into Eq. (B2):

$$F(AH + r) = I_0 \cos \frac{\pi}{4} \left(1 - \frac{\Delta x}{x}\right), \quad (\text{B4})$$

where

$$\Delta x = L_x \tan \theta. \quad (\text{B5})$$

Using Eqs. (B1) and (B5) in Eq. (B4), one derives

$$F(r) = I_0 \cos \frac{\pi}{4} [1 - C_1 \tan(C_2 r)], \quad (\text{B6})$$

where $C_1 = (L_x/x) \cos(\pi/4)$ and $C_2 = (1/L_j) \cos(\pi/4)$.

¹P. E. Nordal and S. Kanstad, "Photothermal radiometry," *Phys. Scr.* **20**, 659 (1979).

²P. E. Nordal and S. Kanstad, "New developments in photothermal radiometry," *Infra. Phys.* **25**, 295–304 (1985).

³A. Melnikov, A. Mandelis, J. Tolev, P. Chen, and S. Huq, "Infrared lock-in carrierography (photocarrier radiometric imaging) of Si solar cells," *J. Appl. Phys.* **107**(11), 114514 (2010).

⁴A. Othonos, M. Nestoros, D. Palmerio et al., "Photothermal radiometry on nickel (pigmented aluminium oxide) selective solar absorbing surface coatings," *Sol. Energy Mater. Sol. Cells* **51**(2), 171 (1998).

⁵I. A. Vitkin, "Biophysical studies of pulsed photothermal radiometry in tissues and tissuelike media," *Med. Phys.* **24**(12), 2056 (1997).

⁶A. Gijbsbertsen, D. Bicanic, J. L. W. Gielen et al., "Rapid, non-destructive and non-contact inspection of solid foods by means of photothermal radiometry; thermal effusivity and initial heating coefficient," *Infrared Phys. Technol.* **45**(2), 93 (2004).

- ⁷I. Kaufman, P. T. Chang, H. S. Hsu *et al.*, "Photothermal radiometric detection and imaging of surface cracks," *J. Nondestruct. Eval.* **6**(2), 87 (1987).
- ⁸G. Busse, D. Wu, and W. Karpen, "Thermal wave imaging with phase sensitive modulated thermography," *J. Appl. Phys.* **71**(8), 3962 (1992).
- ⁹D. Wu and G. Busse, "Lock-in thermography for nondestructive evaluation of materials," *Rev. Gén. Therm.* **37**(8), 693 (1998).
- ¹⁰W. P. Leung and A. C. Tam, "Thermal conduction at a contact interface measured by pulsed photothermal radiometry," *J. Appl. Phys.* **63**(9), 4505 (1988).
- ¹¹T. T. N. Lan, U. Seidel, and H. G. Walther, "Theory of microstructural depth profiling by photothermal measurements," *J. Appl. Phys.* **77**(9), 4739 (1995).
- ¹²T. T. N. Lan, U. Seidel, H. G. Walther *et al.*, "Experimental results of photothermal microstructural depth profiling," *J. Appl. Phys.* **78**(6), 4108 (1995).
- ¹³C. Wang, A. Mandelis, and Y. Liu, "Photothermal radiometry with solid cylindrical samples," *J. Appl. Phys.* **96**(7), 3756 (2004).
- ¹⁴C. Wang, A. Mandelis, and Y. Liu, "Thermal-wave nondestructive evaluation of cylindrical composite structures using frequency-domain photothermal radiometry," *J. Appl. Phys.* **97**(1), 014911 (2005).
- ¹⁵C. Wang, A. Mandelis, Y. Liu *et al.*, "Frequency domain photothermal radiometry with spherical solids," *J. Appl. Phys.* **101**(8), 659 (2007).
- ¹⁶G. Xie, Z. Chen, C. Wang *et al.*, "Laser induced thermal-wave fields in bilayered spherical solids," *Rev. Sci. Instrum.* **80**(3), 1113 (2009).
- ¹⁷G. Xie, J. Zhang, L. Liu *et al.*, "Thermal conductivity depth-profile reconstruction of multilayered cylindrical solids using the thermal-wave Green function method," *J. Appl. Phys.* **109**(11), 973 (2011).
- ¹⁸A. Mandelis, *Diffusion-Wave Fields: Mathematical Methods and Green Functions* (Springer, New York, 2001).
- ¹⁹A. Salazar and R. Celorrio, "Application of the thermal quadrupole method to the propagation of thermal waves in multilayered cylinders," *J. Appl. Phys.* **100**(11), 3756 (2006).
- ²⁰N. Madariaga and A. Salazar, "Propagation of thermal waves in multilayered spheres," *J. Appl. Phys.* **101**(10), 3756 (2007).
- ²¹R. Tai, J. Zhang, C. Wang, and A. Mandelis, "Thermal-wave fields in solid wedges using the Green function method: Theory and experiment," *J. Appl. Phys.* **113**(13), 133501 (2013).
- ²²F. P. Incropera, *Fundamentals of Heat and Mass Transfer*, 3rd ed. (Wiley, New York, 1990).
- ²³M. Abramowitz and I. A. Stegun, *Handbook of Mathematical Functions, with Formulas, Graphs, and Mathematical Tables* (Dover Publications, 1964).